PAPER

Electrically reconfigurable MoO_3/InSe van der Waals heterojunctions

2D Materials

PAPER

RECEIVED
3 September 2024

REVISED
9 October 2024

ACCEPTED FOR PUBLICATION
21 October 2024

PUBLISHED
30 October 2024

Electrically reconfigurable MoO_3/InSe van der Waals heterojunctions

Jiancui Chen[1,2,4], Peng Song[1,2,4], Chijun Wei[2], Kang Wu[1,2], Hao Wang[1,2], Xuanye Liu[1,2], Hui Gao[1,2], Hui Guo[1,2,3], Haitao Yang[1,2,3,*], Lihong Bao[1,2,3,*] and Hong-Jun Gao[1,2,3]

[1] Institute of Physics, Chinese Academy of Sciences, Beijing 100190, People's Republic of China
[2] School of Physical Sciences and CAS Key Laboratory of Vacuum Physics, University of Chinese Academy of Sciences, Beijing 100049, People's Republic of China
[3] Hefei Nationals Laboratory, Hefei, Anhui 230088, People's Republic of China
[4] These authors contribute equally: Jiancui Chen, Peng Song.
[*] Authors to whom any correspondence should be addressed.

E-mail: htyang@iphy.ac.cn and lhbao@iphy.ac.cn

Keywords: two-dimensional materials, van der Waals heterostructure, type-III band alignment, rectification, photodetection

Supplementary material for this article is available online

Abstract

Van der Waals (vdW) heterojunctions formed by stacking different layers of two-dimensional atomic crystals with atomically sharp interface and versatile band alignment have been considered as promising candidates for construction of nanoelectronic and nanophotonic devices. Here, we demonstrate the electrically reconfigurable behavior in MoO_3/indium selenide (InSe) vdW heterojunction with a type-III broken-gap band alignment. The electrical reconfigurability is enabled by the ambipolar transport property of InSe, which is achieved through the use of Pt as contact electrodes. By electrostatically doping the InSe, the reconfigurable MoO_3/InSe heterojunctions can be converted between *p*-*n* and n^+-*n* junctions. As a current rectifier, the MoO_3/InSe heterojunction shows rectification ratios of $\sim 10^7$ and $\sim 10^4$ for forward and backward bias conditions, respectively. As a photodetector, the MoO_3/InSe heterojunction shows stable photo-switching behavior with a $\sim 10^5$ on/off ratio and an ultralow dark current ($\approx$10 fA). The response time is measured to be 500 μs and 300 μs for rise and fall processes, respectively. These results highlight the role of MoO_3 with high electron affinity in construction of vdW heterostructure with type-III band alignment and provide a new platform for high performance optoelectronic devices.

1. Introduction

Since the discovery of graphene, two-dimensional (2D) materials have rapidly established themselves as intriguing building blocks for electronic applications [1–3]. van der Waals (vdW) heterostructures, formed by stacking different kinds of 2D materials with strong in-plane covalent bonds and weak out-of-plane vdW forces, possess unusual properties due to the atomically sharp interface and diverse band alignment [4–6]. In general, there are three kinds of energy band alignment for the heterostructures, including straddling band alignment (type-I), staggered band alignment (type-II), and broken-gap band alignment (type-III). For the type-I band offsets, both the holes and electrons accumulate in one side at the interface which can assists a 2D electron gas [7] or promotes carrier recombination in the solar cell [8]. For the type-II and type-III band offsets, the holes and electrons are separated into different components which are essential for the electronic devices such as rectifying junction [9] and optoelectronic devices [10]. In particular, the type-III heterostructures have a non-overlapping band gap between the two semiconductors, resulting in the charge transport across the heterostructures via band-to-band tunneling, which shows great potential for applications in transistors[11], diode [12], or optoelectronic devices [13]. The heterostructures with type-III band alignment based on $SnSe_2$/WSe_2, shows a subthreshold swing of 37 mV·dec^{-1} in transistors, an ultrahigh rectification ratio of 10^8 in diodes [14], a peak-to-valley ratio of 4

in negative differential resistance phenomenon [13]. The combination of PtS_2 and WSe_2 shows a rectification ratio $\sim 10^8$, a large photocurrent on/off ratio over 10^5 [15]. Although the past studies on the broken-gap band alignment heterostructure are significant and intense, recent advances in this realm are limited by the material choice due to their fixed band structures.

α-phase molybdenum trioxide (α-MoO_3) as a layered semiconductor with large electron affinity ($\sim$6.7 eV) and degenerate *n*-type doping can form type-III heterostructure with a broad range of 2D materials [16, 17]. α-MoO_3 is a wide band gap semiconductor ($\sim$2.9 eV) with an orthorhombic crystal structure consisting of unique double layers of distorted MoO_6 octahedral units [18]. The bottom of the conduction band of the MoO_3 is much higher than the top of the valence band of semiconductors like BP, transition metal dichalcogenides, and metal chalcogenide [17, 19]. The unique band structure makes it an attractive candidate in the construction of broken-gap band structure with other 2D materials. Nevertheless, the study on the type-III band alignment heterostructure based on the combination of MoO_3 and other 2D materials still remain elusive.

In this work, we demonstrate MoO_3/indium selenide (InSe) vdW heterojunction with type-III band alignment can be electrically configured for current rectification and photodetection applications, which is enabled by the realization of ambipolar transport behavior in InSe flakes using Pt as contact metal [20]. The MoO_3/InSe heterojunctions can be converted between *p*-*n* and n^+-*n* junctions depending on the doping of InSe flakes by the electrostatic gating. The *p*-*n* and n^+-*n* junctions demonstrate excellent properties with diverse electronics and optoelectronics applications. The rectification ratio of the forward and backward rectifier diode in *p*-*n* junction reaches $\sim 10^7$ and 10^4, respectively. In addition, upon a 450 nm laser illumination, the MoO_3/InSe heterojunction exhibits a comparable current on/off ratio $\sim 10^5$. Moreover, an ultralow dark current $\approx$10 fA has been achieved. The photo-response time for rise and fall processes is measured to be 500 μs and 300 μs, respectively.

2. Result and discussion

Figure 1(a) shows a schematic of the MoO_3/InSe heterostructure on a 280 nm SiO_2/Si substrate. The graphite serves as the gate electrode of the device. Hexagonal boron nitride (hBN) is chosen to be the dielectric of the device for its low carrier scattering effect and reliable dielectric properties [21, 22]. Pt/Au (7 nm/70 nm) metal stacks on the MoO_3 and InSe serve as source (s) and drain (d), respectively. The MoO_3 layer is grounded. Drain voltage (V_{ds}) and gate voltage (V_{gs}) are applied to the InSe and graphite, respectively. Figure 1(b) shows the typical optical image of the MoO_3/InSe heterostructure device. The edges of the graphite, hBN, MoO_3 and InSe are marked by dotted lines with green, blue, red, and purple, respectively. Graphite, hBN, MoO_3, and InSe were transferred onto heavily p-doped silicon substrate in sequence using mechanical exfoliation and the dry-transfer method [20, 23]. The detailed transfer process and MoO_3 single crystal growth are described in the experimental section. The optical image of the as-grown MoO_3 single crystal is shown in the supplementary figure S1. The high quality single crystal MoO_3 has been characterized by the x-ray diffraction and Raman spectra, which is shown in the supplementary figure S2a and S2b, respectively. The Raman spectrum of the InSe flake on the SiO_2/Si substrate shown in the figure S2c is consistent with the previous result [24]. The thicknesses of the MoO_3 and InSe flakes were measured to be $\sim$21 and $\sim$32 nm by atomic force microscopy, respectively, as shown in supplementary figure S3.

Before the characterization of electrical transport properties of MoO_3/InSe heterojunction, the electrical properties of the MoO_3 and InSe field-effect transistors (FETs) are studied. Figure 1(c) shows the transfer curves of the MoO_3 FET. For different drain-source voltages (V_{ds} = 0.1 V, 1 V, 0.5 V, and 2 V) and sweeping gate voltages (V_{gs}) from -6 V to 6 V, the current almost keeps constant, indicating a weak gate modulation behavior. This is attributed to the spontaneous generation of abundant oxygen vacancies in MoO_3 under an oxygen-free environment, which introduces doping energy levels close to the conduction band and the heavily *n*-doping in MoO_3 [25]. The almost linear output curves of the MoO_3 FETs with V_{ds} ranging from -5 V to 5 V present good ohmic contact between MoO_3 and Pt, as shown in supplementary figure S4a. The transfer curves of the InSe FETs for V_{ds} = 0.5 V and 1 V are shown in figure 1(d). An ambipolar transport behavior with a large on/off current ratio of $\sim 10^7$ for both holes and electrons is clearly observed. When V_{ds} increases from 0.5 V to 1 V, the off-state current increases while the threshold voltage decreases, which is due to the well-known gate-induced drain leakage and drain-induced barrier lowering effect, respectively [14, 26, 27]. The output curves of the InSe FETs under different gate voltages are shown in the supplementary figure S4b, in which the non-linear behavior indicates the formation of Schottky contacts between InSe and Pt.

Figure 2(a) shows the energy band diagram of InSe and MoO_3 before contact, revealing that the bottom of conduction band of MoO_3 is much higher than the top of valence band of InSe. Therefore, the MoO_3/InSe heterostructure has an obvious Type-III broken-gap band alignment after contact. This is verified by the backward rectification behavior

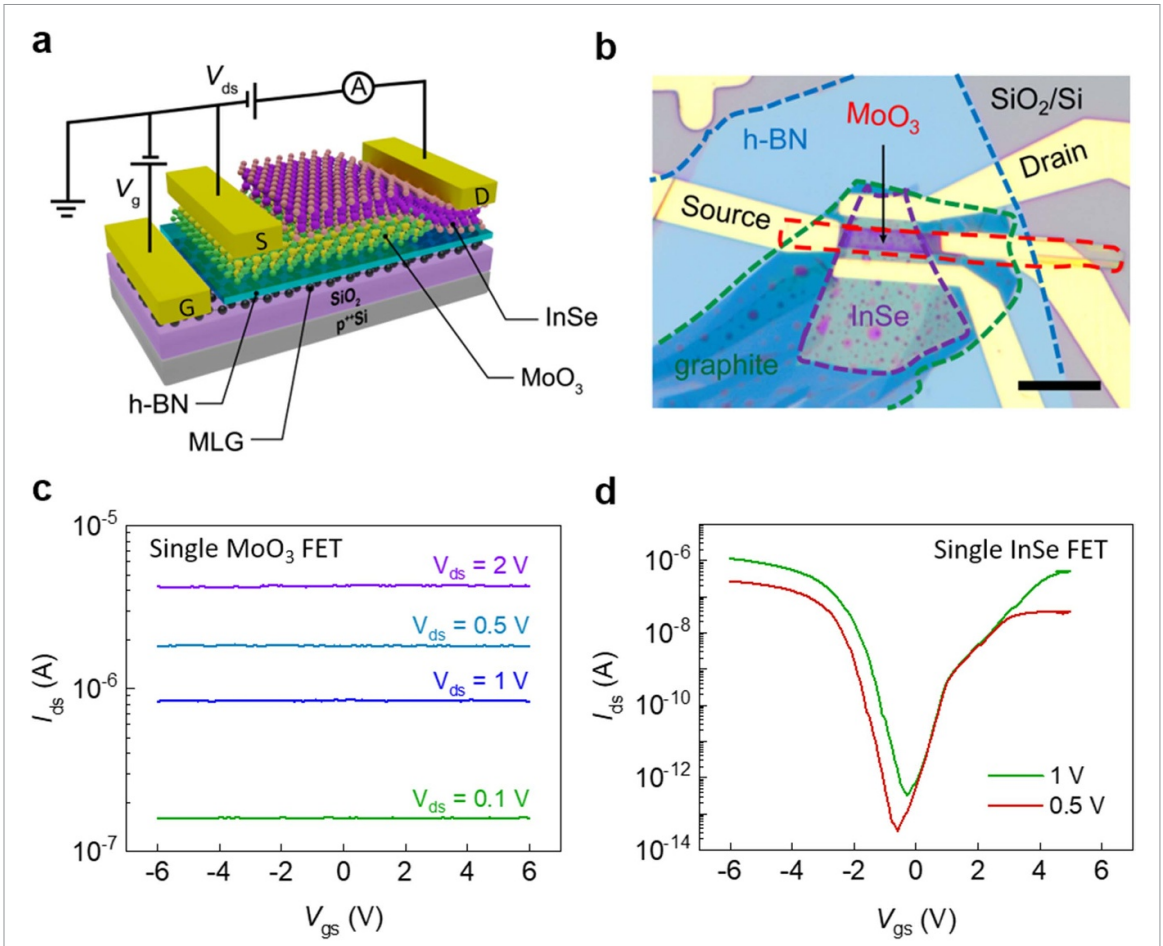

Figure 1. The device structure and electrical properties of the MoO_3 and InSe. (a) 3D schematic structure of the MoO_3/InSe heterostructure device. The substrate is 280 nm SiO_2 on the top of a heavily *p*-doped silicon. The source electrode on the MoO_3 flake and drain electrodes on the InSe flake are Pt/Au (7/70 nm). (b) The typical optical image of the device. The edges of the graphite, h-BN, MoO_3 and InSe are marked by dotted lines with green, blue, red, and purple, respectively. The scale bar is 10 μm. (c) Transfer curves of the MoO_3 FET (I_{ds}–V_{gs}) on logarithmic scale, showing weak gate modulation. (d) Transfer curves of the InSe FET on logarithmic scale, showing ambipolar transport behavior.

in the output characteristics (I_{ds}–V_{ds} curve) of the MoO_3/InSe heterojunction without the gate modulation (V_{gs} gloating), as shown in figure 2(b). When lowering the barrier height at positive drain bias by introducing hole doping, such as setting $V_{gs} = 0$ V, the forward current of the MoO_3/InSe heterojunction increases, as shown in figure 2(c). Figures 2(d) and (e) show the output characteristics of the MoO_3/InSe heterojunction with V_{ds} ranging from −2 V to +2 V under positive and negative gate voltage (V_{gs}) modulation, respectively. As shown in figure 2(d), when sweeping V_{gs} from −6.5 V to −8.5 V in a step of −0.5 V, InSe is heavily doped by holes (figure 1(d)) and the MoO_3/InSe heterojunction works as a *p*-*n* junction, showing forward rectification characteristics. The inset in figure 2(d) shows the output curves of the MoO_3/InSe *p*-*n* heterojunction on logarithmic scale, revealing a rectification ratio of up to $\sim 10^7$. An ideality factor η of 2.4 is extracted from the ideal diode region. The ideality factor of a diode typically varies between 1 and 2 depending on the relative contribution of current from diffusion and recombination, respectively [28, 29]. The high value extracted for the ideality factor indicates dominant contribution from recombination current at the MoO_3/InSe junction. When sweeping V_{gs} from 3 V to 4 V, InSe is doped by electrons and the MoO_3/InSe heterojunction works in an n^+-n junction mode, showing backward rectifying characteristics, as shown in figure 2(e). The inset of figure 2(e) shows the output curves of the MoO_3/InSe n^+-n heterojunction on the logarithmic scale, clearly showing a backward current rectification ratio of up to $\sim 10^4$. An ideality factor of ∼1.3 is extracted, suggesting the diffusion current dominates in n^+-n junction. The forward rectification under positive V_{gs} and backward rectification under negative V_{gs} in the MoO_3/InSe heterojunction are also observed in the other device, as shown in supplementary figure S5, indicating the reproducibility of this behavior. To confirm the formation of *p*-*n* and n^+-n junctions for the MoO_3/InSe heterostructure under different electrostatic doping

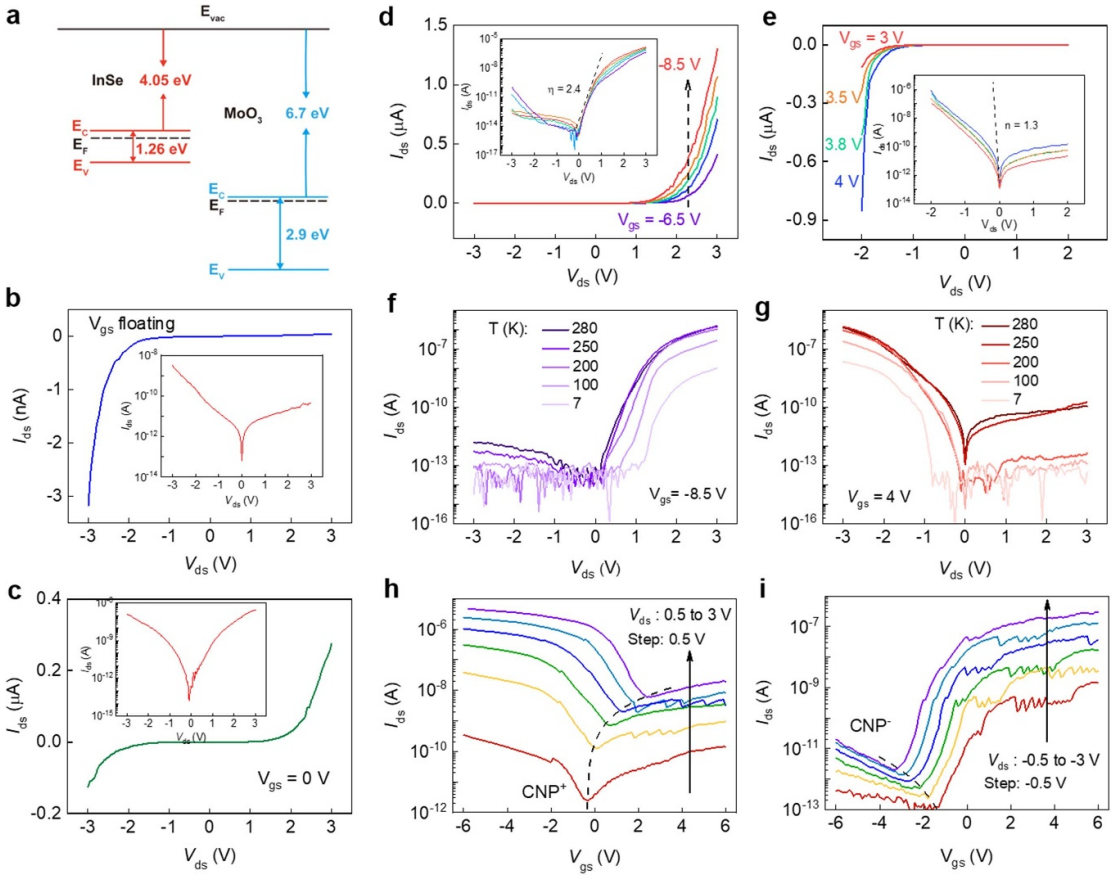

Figure 2. Electrical characterization of the MoO_3/InSe heterojunction. (a) The energy band diagram of InSe and MoO_3 before contact, showing type-III broken-gap band alignment in the MoO_3/InSe heterostructure. (b) Output characteristics of the MoO_3/InSe heterojunction with back-gate floating, showing the backward rectification behavior. (c) Output characteristics of the MoO_3/InSe heterojunction with $V_{gs} = 0$ V. (d) Output characteristics of the MoO_3/InSe heterojunction when sweeping V_{gs} from −8.5 V to −6.5 V in a step of −0.5 V, showing forward rectifying behavior. The inset is the output curves of the MoO_3/InSe heterojunction on the logarithmic scale, showing the rectification ratio up to $\sim 10^7$. (e) Output characteristics of the MoO_3/InSe heterojunction when sweeping V_{gs} from 3 V to 4 V, showing backward rectifying behavior. The inset shows the output curves on the logarithmic scale, indicating a rectification ratio up to $\sim 10^4$. (f)–(g) The output curves of the MoO_3/InSe *p*-*n* heterojunction with $V_{gs} = -8.5$ V (f) and *n*+-*n* heterojunction with $V_{gs} = 4$ V (g) at different temperatures, respectively. (h) Transfer characteristics of the MoO_3/InSe heterojunction at different V_{ds} ranging from 0.5 V to 3 V in a step of 0.5 V. The CNP^+ represents the charge neutral point where the majority carriers change from holes to electrons at $V_{ds} > 0$. (i) Transfer characteristics of the MoO_3/InSe heterojunction at different V_{ds} from −0.5 V to −3 V in a step of −0.5 V. The CNP^- represents the charge neutral point where the majority carriers change from electrons to holes at $V_{ds} < 0$.

conditions, the temperature-dependent output characteristics is measured, as shown in figures 2(f) and (g), respectively. For the forward rectifying diode ($V_{gs} = -8.5$ V) (figure 2(f)), with increasing temperatures from 200 K to 280 K, the reverse leakage current increases, which can be attributed to temperature-assisted carrier tunneling owing to the decreases of the barrier height at the MoO_3/InSe interface. The forward current shows a relatively independent behavior with temperature from 200 K to 280 K, implying that the thermal emission current barely exists. For the backward rectifying junction (figure 2(g)), at -1.4 V $< V_{ds} < 0$ V, the reverse current decreases sharply for temperatures range from 250 K to 200 K, implying the existence of the thermal emission current. However, at $V_{ds} < -1.4$ V, the current shows a relatively independent behavior with the temperature from 200 K to 280 K, indicating the existence of the tunneling current. By increasing the backward current and decreasing the forward leakage current, a rectification ratio $\sim 10^7$ can be realized. Figures 2(h) and (i) show the transfer characteristics (I_{ds}–V_{gs} curve) of the MoO_3/InSe heterojunction under positive (figure 2(h)) and negative V_{ds} (figure 2(i)), respectively. Ambipolar transport behavior in the MoO_3/InSe heterojunction under both positive and negative V_{ds} is clearly observed. CNP^+ and CNP^- represent the charge neutral point where the majority carriers change from holes to electrons at $V_{ds} > 0$ (figure 2(h)) and from electrons to holes at $V_{ds} < 0$ (figure 2(i)), respectively. When $V_{gs} < V_{NCP}{}^-$, the heterostructure will show the forward-type rectifying behavior. The rectification ratio increases by decreasing the gate voltage as shown in figure 2(d). When $V_{CNP}{}^- < V_{gs} < V_{CNP}{}^+$, the current of the heterostructure will increase with both

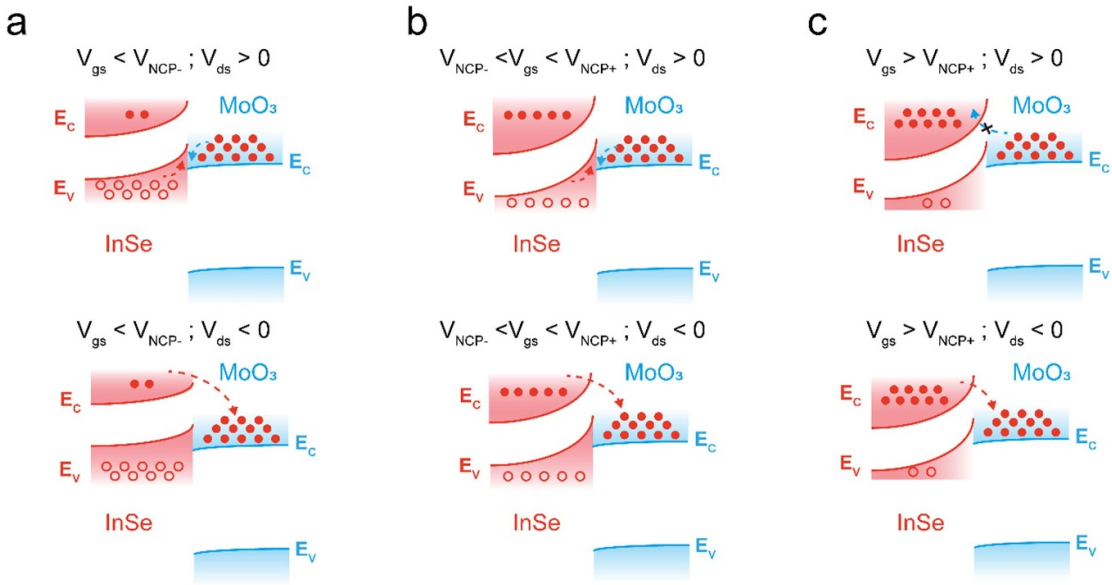

Figure 3. The schematic of the energy band alignment diagram of MoO_3/InSe heterojunction under different gate and drain voltage bias conditions. (a) When $V_{gs} < V_{CNP}^-$, the InSe layer is electrically *p*-type doped at both positive and negative drain biases. Electrons are injected from MoO_3 into InSe to recombine with the holes at $V_{ds} > 0$ V. When $V_{ds} < 0$ V, the MoO_3/InSe junction is depleted. (b) When $V_{CNP}^- < V_{gs} < V_{CNP}^+$ and $V_{ds} > 0$ V, the InSe will be doped by holes. The current (I_{ds}) is dominated by the recombination process. When $V_{CNP}^- < V_{gs} < V_{CNP}^+$ and $V_{ds} < 0$ V, the InSe will be doped by electrons. The current (I_{ds}) is dominated by the thermionic emission process. (c) When $V_{gs} > V_{CNP}^+$, the InSe layer will be electrically *n*-type doped. Electrons tunnel or thermally emission from InSe into MoO_3 at $V_{ds} < 0$ V. When $V_{ds} > 0$ V, the MoO_3/InSe junction is depleted.

positive and negative drain bias. When $V_{gs} > V_{CNP}^+$, the heterostructure shows backward rectifying behavior as shown in figure 2(e).

Figure 3 shows the schematic of the energy band alignment diagram of the MoO_3/InSe heterojunction under different gate and drain voltage bias conditions. As shown in figure 3(a), when $V_{gs} < V_{CNP}^-$, the InSe layer is electrically *p*-type doped at both positive and negative drain bias. At $V_{ds} > 0$, the holes will be injected from InSe into MoO_3, whereas the electrons will be injected from the MoO_3 into InSe. As the holes and electrons reach the junction area, they recombine with each other or overcome the barrier. Considering the band alignment between InSe and MoO_3, the barrier height is larger than 1.2 eV, which is too high for the carriers to overcome. Therefore, the current is dominated by recombination process, which has also been observed in other type-III heterostructure systems [14, 30, 31]. While at $V_{ds} < 0$, the applied and built-in electric fields are in the same direction, resulting in the widening of the depletion region and the low current state. As shown in figure 3(b), when $V_{CNP}^- < V_{gs} < V_{CNP}^+$, the InSe layer is electrically *p*-type doped for $V_{ds} > 0$ and *n*-type doped for $V_{ds} < 0$. At $V_{ds} > 0$, the carriers will recombine at the junction area. While at $V_{ds} < 0$, the electrons can overcome the barrier by thermal emission, leading to a high current state. When $V_{gs} > V_{CNP}^+$, as shown in figure 3(c), the InSe layer is electrically n-type doped. For $V_{ds} > 0$, it is difficult for the electrons to tunnel or overcome the high and wide barrier at the MoO_3/InSe interface, resulting in a low current state. While for $V_{ds} < 0$, the electrons can overcome or tunnel the low and narrow barrier between MoO_3 and InSe, resulting in a high current state. By varying the gate and drain voltage biases, the MoO_3/InSe heterojunction can behave as forward or backward rectifying diodes, as shown in figures 2(d) and (e).

The successful electrical reconfiguration of MoO_3/InSe heterojunctions, both for *p*-*n* and n^+-*n* junctions, enables their function as elementary devices for optoelectronic applications. Figure 4(a) shows the forward current of the rectifier diode (p-n junction) illuminated by various laser ($\lambda = 450$ nm) powers at $V_{gs} = -8$ V, showing that the forward current will decrease dramatically with increasing laser power. Conversely, the backward current increases with increasing laser power, as shown in figure 4(b). When illuminated, photons with energy exceeding the bandgap of InSe are absorbed, leading to the formation of electron-hole pairs that are separated by the applied drain bias [32, 33]. The photo-generated free electrons and holes drift in opposite directions towards the source and drain, respectively, resulting in an increase in the current under negative V_{ds}. Nevertheless, the photo-generated electrons and holes pairs prevent the recombination of the electron and holes at the interface of the InSe and MoO_3 flake, thereby reducing the current under positive V_{ds}, as schematically shown in supplementary figure S6. Figure 4(c) shows the $|I_{ds}|-V_{gs}$ behaviors of the heterostructure at $V_{ds} = -2$ V, without illumination and

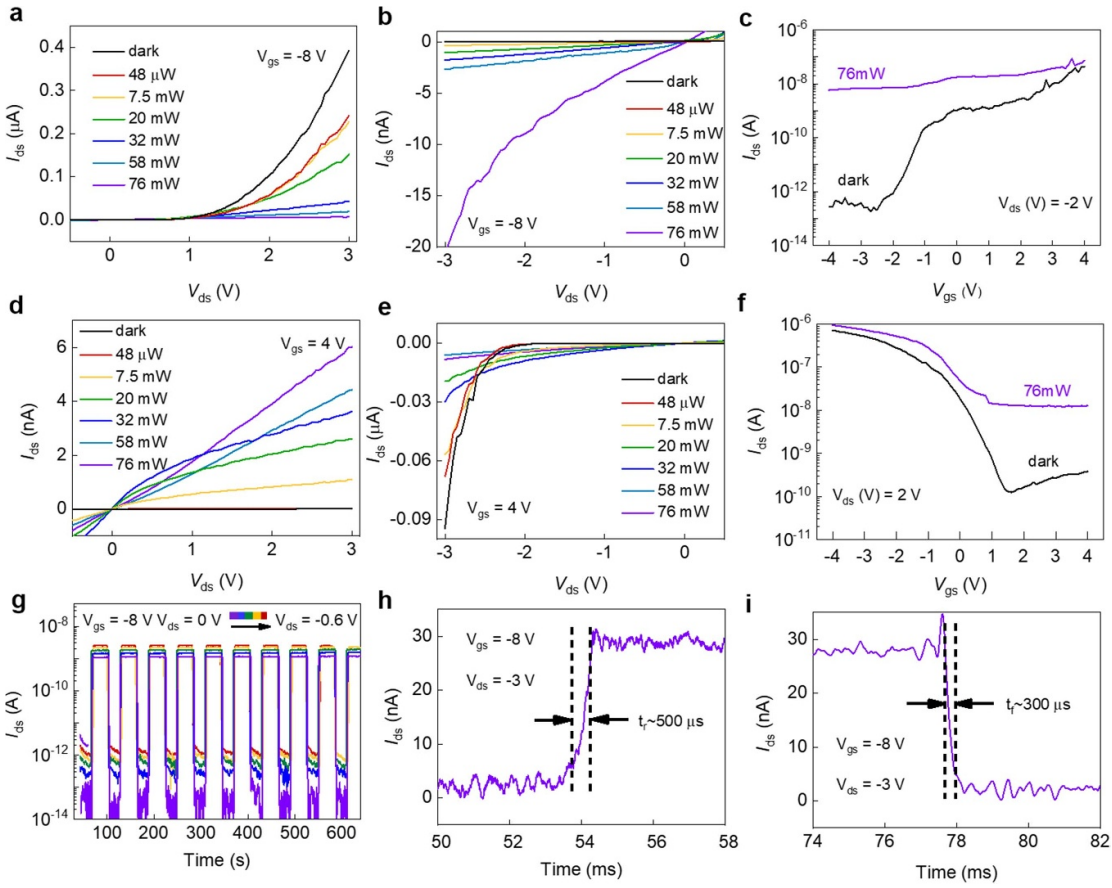

Figure 4. Photoresponse characteristics of the MoO_3/InSe heterojunction. (a) And (b) the I_{ds}–V_{ds} curves at $V_{ds} > 0$ (a) and $V_{ds} < 0$ (b) of the *p*-*n* junction at $V_{gs} = -8$ V under 450 nm laser illumination with different power levels. (c) The $|I_{ds}|-V_{gs}$ curves of the heterostructure at $V_{ds} = -2$ V under dark environment and 450 nm laser illumination with a power intensity of 76 mW. (d) And (e) the I_{ds}–V_{ds} curves at $V_{ds} > 0$ (d) and $V_{ds} < 0$ (e) of the n^+-*n* junction at $V_{gs} = 4$ V under 450 nm laser illumination with different power levels. (f) The $|I_{ds}|$–V_{gs} curves of the heterostructure at $V_{ds} = 2$ V under dark environment and 450 nm laser illumination with a power intensity of 76 mW. (g) 10 cycles of time-dependent photoresponse of the *p*-*n* junction under 450 nm laser illumination with a power intensity of 76 mW at $V_{gs} = -8$ V and V_{ds} varying from 0 to −0.6 V in step of −0.2 V. (h) And (i) time-resolved photoresponse of the device under 450 nm laser illumination at $V_{ds} = -3$ V for the rising (h) and falling (i) process, respectively.

illuminated by laser powers of 76 mW, respectively. The current with illuminating laser decays slowly as decreasing gate voltage and I_{photo}/I_{dark} reaches up to 10^4 at $V_{gs} = -4$ V. Figures 4(d) and (e) show the backward current of the diode (n^+-*n* junction) illuminated by various laser powers at $V_{gs} = 4$ V. In contrast to that of *p*-*n* junction (figures 4(a) and (b)), the forward current increases with the increasing laser power (figure 4(d)), while the backward current decreases with the increasing laser power (figure 4(e)). This is attributed to the migration of photo-generated free electrons and holes towards the drain and source under laser illumination, resulting in an increase in the current under positive V_{ds}. When $V_{ds} < 0$, the high energy barrier at the interface between MoO_3 and InSe traps the photo-generated holes in localized states near the valence band edge, inducing a gating effect. Figure 4(F) shows the $|I_{ds}|-V_{gs}$ behaviors of the n^+-*n* junction at $V_{ds} = 2$ V, without illumination and illuminated by laser powers of 76 mW, respectively. The current with illuminating laser decays dramatically as increasing gate voltage, indicating a strong gate modulation behavior. To further explore the performance of the MoO_3/InSe heterostructure as a photodetector, a stable photo-switching behavior is exhibited in figure 4(g) under a 76 mW laser illuminating, with $V_{gs} = -8$ V and V_{ds} varying from 0 to −0.6 V in steps of −0.2 V. The I_{photo}/I_{dark} can reach to be 10^5 and the dark current is reduced to ~10 fA. The rise time (t_r) in figure 4(h) and fall time (t_f) in figure 4(i) are measured as 500 μs and 300 μs, respectively. The responsivity, detectivity, and quantum efficiency, which are three figures of merit characterizing the performance of phototransistors, are presented in supplementary table S1. These results demonstrate the excellent performance of the MoO_3/InSe heterostructure as a photodetector, exhibiting high sensitivity and fast response times.

3. Conclusion

In summary, by electrically conversion of the ambipolar transport behavior of InSe, we have successfully fabricated type-III MoO_3/InSe heterostructure device which can function as forward rectifier diode (*p*-*n* junction) and backward rectifier diode (n^+-*n* junction) with high rectification ratio of $\sim 10^7$ and $\sim 10^4$, respectively. As a photodetector, the device demonstrates a stable photo-switching behavior, achieving a high photo-dark current ratio of $\sim 10^5$, an ultra-low dark current of 10 fA, and fast response times of 500 μs for rise process and 300 μs for fall process. These remarkable results demonstrate the versatile functionalities of type-III band energy alignment heterostructure based on MoO_3 and InSe, affording new opportunities for further research and applications on the broken-gap heterostructures.

4. Experimental section

Synthesis of molybdenum oxide single crystal: The *a*-MoO_3 single crystal was synthesized by physical vapor deposition method using a tube furnace with open ends. The diameter of the tube furnace is 26 mm. The MoO_3 powder with a purity of 99.998% (Alfa Aesar) and weight of 0.2 g as source was placed at the center of a quartz tube. To obtain high-quality *a*-MoO_3 single crystal, the tube furnace was firstly heated up to 760 °C in 20 min and maintained for 11 h, during which the MoO_3 powder was sublimated and recrystallized onto the low-temperature regions of the quartz tube. Secondly, the recrystallized MoO_3 was collected and placed at the center of the tube. The tube furnace was heated up to 760 °C in 20 min and maintained for 11 h again. After repeat the second step for three times, the final recrystallized MoO_3 deposited on the low-temperature regions of the quartz tube were collected for further characterization. The optical image of the as-grown MoO_3 single crystal is shown in the figure S1. The scale in the direction of [100] can reach 5 mm and 12 mm in [001].

Materials characterization: The morphology of the MoO_3, graphite, BN, and InSe was characterized by optical microscope (Olympus BX51-SC30). Raman spectrum of the MoO_3 and InSe were conducted on samples under ambient conditions with and excitation wavelength of 532 nm using a commercial Raman spectrometer (WITec alpha 300R). The XRD patterns were collected using a Rigaku SmartLab SE with monochromatic Cu Kα as radiation source ($\lambda = 0.154$ nm). The thickness of MoO_3, InSe, and h-BN were determined by Asylum Research Cypher S AFM after electrical measurements.

Preparation of MoO_3/InSe heterostructures: MoO_3/InSe heterostructures were prepared by mechanical exfoliation and dry-transfer method. Graphite was exfoliated on a 280 nm SiO_2/Si substrate. Whereas, BN, MoO_3 and InSe were exfoliated onto three individual pieces of polydimethylsiloxane (Gel Park). Then, the target BN flake was transferred onto the graphite. The target MoO_3 was placed onto the graphite/BN flakes. The InSe was transferred onto the MoO_3/graphite/BN flakes on the substrate. Finally, the substrate was heated to remove the bubbles into the substrate. The material exfoliation and transfer processes were done in an argon-filled glovebox.

Device Fabrication: Polymethyl Methacrylate (PMMA 950 A5) was used as a lithography resist. Contact patterns were fabricated by standard e-beam lithography. Then, the e-beam evaporation process was utilized to form the contact electrode (Pt/Au). After that, the lift-off process was performed to remove the PMMA using acetone.

Electrical Characterization: The electrical properties of the MoO_3 FETs, InSe FETs, and MoO_3/InSe heterostructure devices were measured by using a Keithley 4200 semiconductor characterization system and a Lakeshore probe station. The optoelectronic performance of MoO_3/InSe heterostructure devices were measured by the same equipment system with a 450 nm wavelength light illuminating. The rise time and fall time of the photo-response were characterized with an oscilloscope (Tektronix MDO4104B-3).

Data availability statement

The data cannot be made publicly available upon publication because no suitable repository exists for hosting data in this field of study. The data that support the findings of this study are available upon reasonable request from the authors.

Acknowledgments

This work was supported by the National Key Research & Development Projects of China (Grant No. 2022YFA1204100), National Natural Science Foundation of China (Grant No. 62488201), CAS Project for Young Scientists in Basic Research (YSBR-003), and the Innovation Program of Quantum Science and Technology (2021ZD0302700).

ORCID iDs

Jiancui Chen https://orcid.org/0000-0002-6267-7821
Lihong Bao https://orcid.org/0000-0002-2942-892X
Hong-Jun Gao https://orcid.org/0000-0002-2088-0522

References

[1] Koppens F H, Mueller T, Avouris P, Ferrari A C, Vitiello M S and Polini M 2014 *Nat. Nanotechnol.* **9** 780–93
[2] Yang H, Heo J, Park S, Song H J, Seo D H, Byun K-E, Kim P, Yoo I, Chung H-J and Kim K 2012 *Science* **336** 1140–3
[3] Liao L, Lin Y-C, Bao M, Cheng R, Bai J, Liu Y, Qu Y, Wang K L, Huang Y and Duan X 2010 *Nature* **467** 305–8

[4] Manzeli S, Ovchinnikov D, Pasquier D, Yazyev O V and Kis A 2017 *Nat. Rev. Mater.* **2** 1–15
[5] Wang M *et al* 2018 *Nat. Electron.* **1** 130–6
[6] Yu W J, Li Z, Zhou H, Chen Y, Wang Y, Huang Y and Duan X 2013 *Nat. Mater.* **12** 246–52
[7] Jin E N, Hardy M T, Mock A L, Lyons J L, Kramer A R, Tadjer M J, Nepal N, Katzer D S and Meyer D J 2020 *ACS Appl. Mater. Interfaces* **12** 52192–200
[8] Selinsky R S, Ding Q, Faber M S, Wright J C and Jin S 2013 *Chem. Soc. Rev.* **42** 2963–85
[9] Lee C-H *et al* 2014 *Nat. Nanotechnol.* **9** 676–81
[10] Chen Y *et al* 2018 *Small* **14** 1703293
[11] Yan X, Liu C, Li C, Bao W, Ding S, Zhang D W and Zhou P 2017 *Small* **13** 1701478
[12] Fan S, Yun S J, Yu W J and Lee Y H 2020 *Adv. Sci.* **7** 1902751
[13] Fan S, Vu Q A, Lee S, Phan T L, Han G, Kim Y-M, Yu W J and Lee Y H 2019 *ACS Nano* **13** 8193–201
[14] Li W, Xiao X and Xu H 2019 *ACS Appl. Mater. Interfaces* **11** 30045–52
[15] Tan C, Yin S, Chen J, Lu Y, Wei W, Du H, Liu K, Wang F, Zhai T and Li L 2021 *ACS Nano* **15** 8328–37
[16] Zhang W-B, Qu Q and Lai K 2017 *ACS Appl. Mater. Interfaces* **9** 1702–9
[17] Xia F, Shao Z, He Y, Wang R, Wu X, Jiang T, Duhm S, Zhao J, Lee S-T and Jie J 2016 *ACS Nano* **10** 10283–93
[18] Chithambararaj A, Rajeswari Yogamalar N and Bose A C 2016 *Cryst. Growth Des.* **16** 1984–95
[19] Liu Y, Stradins P and Wei S-H 2016 *Sci. Adv.* **2** e1600069
[20] Wu L *et al* 2020 *Nano Res.* **13** 1127–32
[21] Ji Y *et al* 2016 *Appl. Phys. Lett.* **108** 012905
[22] Hattori H Y T, Taniguchi T, Watanabe K and Nagashio K 2015 *ACS Nano* **9** 916–21
[23] Wu L *et al* 2021 *Nat. Nanotechnol.* **16** 882–7
[24] Qin F, Gao F, Dai M, Hu Y, Yu M, Wang L, Feng W, Li B and Hu P 2020 *ACS Appl. Mater. Interfaces* **12** 37313–9
[25] Cho Y, Park J H, Kim M, Jeong Y, Ahn J, Kim T, Choi H, Yi Y and Im S 2018 *Adv. Funct. Mater.* **28** 1801204
[26] Chan T Y, Chen J, Ko P K and Hu C 1987 *IEEE Int. Electron Devices Meet* vol 31 pp 718–21
[27] Li H-M, Lee D-Y, Choi M S, Qu D, Liu X, Ra C-H and Yoo W J 2014 *Sci. Rep.* **4** 4041
[28] Chuang S *et al* 2014 *Nano Lett.* **14** 1337–42
[29] Chuang S, Kapadia R, Fang H, Chia Chang T, Yen W-C, Chueh Y-L and Javey A 2013 *Appl. Phys. Lett.* **102** 242101
[30] Roy T, Tosun M, Cao X, Fang H, Lien D-H, Zhao P, Chen Y-Z, Chueh Y-L, Guo J and Javey A 2015 *ACS Nano* **9** 2071–9
[31] Cheng R, Wang F, Yin L, Wang Z, Wen Y, Shifa T A and He J 2018 *Nat. Electron.* **1** 356–61
[32] Wang H, Wu K, Guo H, Gao H, Liu L, Wu L, Chen J, Yang H, Bao L and Gao H-J 2023 *2D Mater.* **10** 035019
[33] Liu L *et al* 2020 *Nano Lett.* **20** 6666–73